
Non-adiabatic intramolecular and photodissociation dynamics studied by femtosecond time-resolved photoelectron and coincidence imaging spectroscopy

O. Gefner,^a E. t.-H. Chrysostom,^b A. M. D. Lee,^{ac} D. M. Wardlaw,^c M.-L. Ho,^d S.-J. Lee,^d B.-M. Cheng,^e M. Z. Zgierski,^a I.-C. Chen,^{*d} J. P. Shaffer,^{*f} C. C. Hayden^{*b} and A. Stolow^{*ac}

^a Steacie Institute for Molecular Sciences, National Research Council, 100 Sussex Drive, Ottawa ON, Canada K1A 0R6. E-mail: albert.stolow@nrc.ca

^b Combustion Research Facility, Sandia National Laboratories, Livermore, CA 94551, USA. E-mail: cchayde@sandia.gov

^c Department of Chemistry, Queen's University, Kingston ON K7L 3N6, Canada

^d Department of Chemistry, National Tsing-Hua University, Hsinchu, Taiwan 300, Republic of China. E-mail: icchen@mx.nthu.edu.tw

^e Synchrotron Radiation Research Center, Hsinchu, Taiwan 300, Republic of China

^f Department of Physics and Astronomy, University of Oklahoma, Norman OK 73019, USA. E-mail: James.P.Shaffer-1@ou.edu

Received 7th January 2004, Accepted 16th January 2004

First published as an Advance Article on the web 7th May 2004

Time-resolved photoelectron spectroscopy (TRPES) is emerging as a useful tool for the study of non-adiabatic dynamics in isolated polyatomic molecules and clusters due to its sensitivity to both electronic and vibrational dynamics. A powerful extension of TRPES, coincidence imaging spectroscopy (CIS), based upon femtosecond time-resolved 3D momentum vector imaging of both photoions and photoelectrons in coincidence, is a new technique for the study of complex dissociative processes. Here we show how these spectroscopies can be used to study both non-adiabatic intramolecular and photodissociation dynamics in polyatomic molecules. Intramolecular dynamics in the α,β -enones acrolein, crotonaldehyde and methyl vinyl ketone are studied using both TRPES and laser-induced fluorescence of HCO(X) product yields. The location of the methyl group is seen to have very dramatic effects on the relative electronic relaxation rates and the HCO(X) yield. Applying both TRPES and CIS to the 200 nm and 209 nm photodissociation of the nitric oxide dimer, (NO)₂, we observe the fs time-scale evolution of the excited parent neutral *via* its photoelectron spectrum and the emergence of the NO(A) photofragment including its energy and angular distributions.

I. Introduction

The non-adiabatic excited state dynamics of polyatomic molecules is the primary step in the photochemistry of many polyatomic molecules.¹ When applicable, high resolution spectroscopy

can provide detailed insights into non-adiabatic intramolecular processes.² In general, however, these problems remain difficult, particularly when the state density becomes high and multi-mode vibronic couplings are involved, as in the famous case of polyenes.³ This situation usually leads to ultrafast non-adiabatic intramolecular dynamics.⁴ As a first step, characterizing the ‘reaction’ pathway can provide a picture of the mechanism and dynamics.^{5,6} The case of photodissociation—when the zeroth order excited states are directly or indirectly coupled to a true continuum, leading to non-adiabatic photodissociation dynamics^{7,8}—is especially challenging. Many photoinduced polyatomic unimolecular reactions are based upon ‘hot molecules’ formed *via* ultrafast internal conversion (IC).

Time-resolved photoelectron spectroscopy (TRPES) is emerging as an important technique for the experimental study of ultrafast non-adiabatic dynamics in polyatomic molecules.^{9–13} Photoelectron spectroscopy is a particularly useful probe of these processes because it is a ‘universal’ probe (*i.e.* no ‘dark’ states) and is sensitive to both electronic configurations and vibrational dynamics. The Koopmans’ picture suggests that emission of an independent outer valence electron occurs without simultaneous electronic reorganization of the ion core. The Koopmans’ correlation rules indicate the cation state expected to be formed upon single photon, single active electron ionisation of a given molecular orbital. Partial ionisation probabilities into specific cation electronic states can differ drastically with respect to the molecular orbital nature of the neutral electronic state. If a given neutral electronic configuration correlates to the ground electronic configuration of the cation, then the photoionisation probability is generally higher than if it does not. This sensitivity has been very successfully exploited in the application of TRPES to the study of ultrafast non-adiabatic dynamics.^{14,15}

In the case of non-adiabatic photodissociation dynamics, it becomes very difficult to ‘follow’ complex excited state dynamics as it proceeds towards dissociation. Hope remains in looking at the product elimination channels in more detail. Examples include studying the time evolution of the product translational and internal energy distributions, angular momentum polarization and other vector correlations. TRPES can be applied as a highly differential probe to these problems by introducing energy-, angle-, time- and mass-resolved photoelectron–photoion coincidence methods. This novel coincidence imaging spectroscopy (CIS) method was demonstrated for the study of NO₂ multiphoton dissociation dynamics, correlating, as a function of time, the NO photofragment energy-angle resolved recoil with photoelectron energy-angle resolved emission.^{16,17} In polyatomic dissociation dynamics, such correlations could shed light on quite complex processes.

In the following, we describe the application of fs TRPES and fs CIS to problems in non-adiabatic intramolecular and photodissociation dynamics. In the area of intramolecular dynamics, we applied TRPES and product yield studies to the study of competing ultrafast processes in some α,β -enones (the simplest of which is propenal). These systems contain both a C=C and a C=O bond and can exhibit complex photochemistry. In the area of photodissociation dynamics, we applied both TRPES and CIS to the study of the nitric oxide dimer, (NO)₂, photodissociation. The paper is organized as follows. An overview of the relevant photophysics and photochemistry of the α,β -enones and the nitric oxide dimer is presented. This is followed by brief descriptions of the experimental approaches. We then present our experimental results from (i) studies of a series of α,β -enones excited to their S₂ state, and (ii) our detailed TRPES and CIS studies of the (NO)₂ photodissociation dynamics at 200 and 209 nm excitation.

II. Ultrafast non-adiabatic intramolecular dynamics: The α,β -enones

The α,β -enones, containing a –C=C–C=O moiety, are bichromophoric systems which exhibit strong interactions between the neighbouring C=C and C=O groups. The conjugative effects of the C=C bond and the inductive effects of the C=O bond lead to a rich and varied photochemistry which includes α -cleavage, H-atom abstraction, [2 π + 2 π] cycloaddition and photochemical rearrangements. Acrolein (propenal)^{18,19} is the simplest of the α,β -enones and provides an important theoretical model for studying configuration interaction involving dynamic electron correlation effects.^{20–22} It additionally provides an important dynamical model of the interplay between competing ultrafast non-adiabatic processes, both IC and intersystem crossing (ISC) in systems

containing interacting $n\pi^*$ and $\pi\pi^*$ states.^{20,21} A simplified picture of α,β -enone excited state processes is shown in Fig. 1.

Ground state acrolein has a central C–C bond of higher bond order than a single bond, due to conjugative effects. This significantly restricts internal rotation and acrolein is found to be (96%) in a planar *s-trans* geometry at room temperature. Analogous to the S_2 (${}^1B_u \pi\pi^*$) transition in *trans*-butadiene, the strongly dipole allowed transition ($f \sim 0.4$) is to the S_2 ($2^1A'$ $\pi\pi^*$) state, a hybrid covalent–ionic (mostly valence) state at 6.4 eV vertical excitation¹⁸ which involves both the C=C and C=O chromophores.²³ Proper treatment of the acrolein S_2 state involves a multi-state dynamical electron correlation treatment of the CASSCF references states in order to avoid artificial Rydberg–valence mixing.²² Due to contributions from both π^* C=C and π^* C=O orbitals and the inductive effect of the C=O bond, the S_2 state is twisted about the C=C bond and involves internal charge displacement due to contributions from $[C^- - C^+ - C=O]$, $[C=C - C^+ - O^-]$, $[C^+ - C^- - C^+ - O^-]$ and $[C^- - C^+ - C^- - O^+]$ resonance structures, leading to a predominant $[C^{\delta+} - C - C - O^{\delta-}]$ form.²¹ The S_2 state adiabatically correlates only with (energetically unavailable) highly excited dissociation products and therefore, as no fluorescence is observed, is assumed to rapidly internally convert to a lower lying singlet state, S_1 .

The S_1 ($1^1A'' n\pi^*$) state at 3.7 eV vertical excitation,^{18,24} by analogy with formaldehyde, is dipole forbidden from the ground state ($f \sim 2 \times 10^{-4}$) and has a planar geometry with a lengthened C–O, as expected for $n_y \rightarrow \pi^*$ excitation localised on the carbonyl group.^{20–22} The S_1 state also has a longer, weaker ethylenic C=C bond and a shorter, stronger aldehydic C–C bond, indicating some reversal of bond order with respect to the ground state.^{20–22} The S_1 state can undergo radiationless transitions to the singlet S_0 ground state and the low-lying triplet T_2 (${}^3A'$ $\pi\pi^*$) and T_1 (${}^3A'' n\pi^*$) states and is therefore central to the complex photochemistry of the α,β -enones.^{20,21} Absorption linewidths measured at the S_1 vibronic origin advocated a (zeroth-order) lifetime of 1.8–2.1 ps, suggested to be due to an ISC to the T_2 (${}^3A'$ $\pi\pi^*$) triplet state at a planar structure near the origin.²⁵ The S_1 state has a conical intersection (CI) with the S_0 ground state at a $\sim 90^\circ$ methylene–twisted geometry located around 15 kcal mol⁻¹ above the S_1 origin.²⁰ It was suggested that, at lower excitation energies, ISC to T_2 should dominate over IC to S_0 .²¹ At much higher energies the S_1 state correlates, but with a large barrier (~ 40 kcal mol⁻¹), to the excited state radical products CH_2CH (${}^2A'$) + HCO (${}^2A''$).²¹

The T_1 (${}^3A'' n\pi^*$) state, like the S_1 state, is planar but with a significantly lengthened C–O bond and intermediate single/double bond character for both C–C bonds,²⁶ comparably reversed with respect to the ground state.^{20–22} This state can correlate with the formation of ground state vinyl and HCO (X) radical products.²⁷ The T_2 (${}^3A'$ $\pi\pi^*$) triplet state has a non-planar geometry and is electronically of biradicaloid nature. The C=O bond order is the same as in S_0 , but the ethylenic

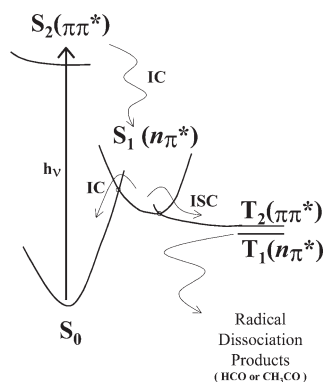
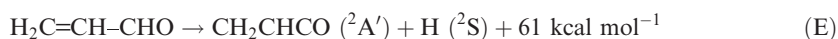
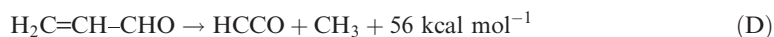
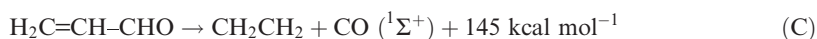
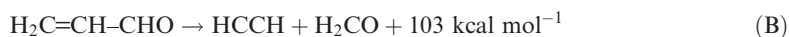
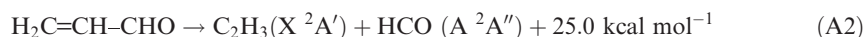
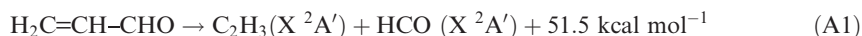


Fig. 1 A schematic picture of ultrafast non-adiabatic processes in the α,β -enones. The optically bright S_2 (${}^1\pi\pi^*$) state rapidly decays *via* an efficient CI to the lower lying S_1 (${}^1n\pi^*$) state. Once on the latter surface, the system may either (1) undergo ‘over the barrier’ IC to the S_0 ground state, eventually dissociating to molecular products or H atoms, or (2) it can experience ultrafast ISC to the T_2 (${}^3\pi\pi^*$) state. The latter may undergo rapid IC to form the near degenerate T_1 (${}^3n\pi^*$) state which can dissociate to form radical products. The competition between ultrafast non-adiabatic processes in the S_1 state determines the fate of the molecule.

C–C bond is greatly changed by the biradical structure—the methylene group is rotated by about 90°. This triplet surface methylene rotation is key to the photochemical conversion of the α,β -enones. The twisting reverses the order of the electronic states, with $T_2(\pi\pi^*)$ dipping below both $S_1(n\pi^*)$ and $T_1(n\pi^*)$ upon methylene rotation, ultimately crossing the S_0 ground state near 90° rotation.^{20–22} This suggests a highly efficient route to hot ground state formation.

The planar ground state of the acrolein cation is of n -hole character and labeled $D_0(n^{-1})$ whereas the first excited cation state, also planar, is of π -hole character, $D_1(\pi^{-1})$.^{28–31} The first twisted excited state of the cation, D_3 , appears at higher energies than we need to consider here. As discussed in more detail below, the complex charge displacement character of the S_2 and S_1 states governs the observed Koopmans' ionisation correlations to the D_0 and D_1 cation states.

The ultraviolet photochemistry of acrolein has been studied experimentally in some detail.^{27,32–39} At 193.4 nm excitation (148 kcal mol⁻¹), the following dissociation channels have been observed:



It should be noted that the $\text{HCO}(\text{A } ^2\text{A}'')$ of channel (A2) is unstable and predissociates to form $\text{H} + \text{CO}$ final products. Channel (B) was observed as a very weak signal and is assumed here to be a minor channel.³⁹ Channels (C) and (D) may be indicative of excited state isomerization to form triplet methyl ketene $\text{CH}_3\text{CHCO}(\text{}^3\text{A}'')$ which then fragments to form vinylidene $\text{CH}_3\text{CH}(\text{}^3\text{A}'') + \text{CO}$ (the former quickly rearranges to ethylene CH_2CH_2). An early photofragmentation translational spectroscopy (PTS) study suggested channel (A1) was the major channel.³⁴ A later PTS study revealed (A1), (C) and (E) as three major channels.³⁶ A detailed laser-induced fluorescence study of the $\text{HCO}(\text{X } ^2\text{A}')$ from channel (A1) revealed that the product state distribution was surprisingly cold as compared to statistical (phase space) theory. This implies that its ground state vinyl radical counterpart contains most of the available energy ($\sim 82\%$) and would undergo secondary dissociation. Furthermore, the $\text{HCO}(\text{X})$ appearance rate ($> 2 \times 10^8 \text{ s}^{-1}$) was much higher than expected from RRKM theory ($\sim 2 \times 10^5 \text{ s}^{-1}$).²⁷ This suggested that there are other, much faster, processes competing with dissociation to radical products on the $T_1(\text{}^3\text{A}'' n\pi^*)$ surface—namely, T_1 IC to $T_2(\text{}^3\text{A}' \pi\pi^*)$ followed by highly efficient ISC, at a twisted geometry, to S_0 . We should also mention that $S_1(\text{}^1n\pi^*)$ to S_0 IC is open at 193 nm excitation and may also compete with triplet state processes. These competing processes could help explain why the $\text{HCO}(\text{X})$ yield from acrolein is much smaller ($\sim 100\times$) than is seen in other systems such as acetaldehyde.³⁷

A recent, unpublished PTS study of acrolein photodissociation at 193 nm used synchrotron VUV radiation for detection/ionisation of photofragment primary and secondary products.³⁹ All of channels (A1), (A2), (B), (C), (D) and (E) were directly observed, although some channels were minor. By observing vinyl radical recoil, these researchers were able to conclude that channel (A2) is quite significant, producing the unstable $\text{HCO}(\text{A})$, and/or that channel (A1) produces significant $\text{HCO}(\text{X})$ above its dissociation limit. If channel (A2) were dominant, this could offer an alternate explanation for the cold $\text{HCO}(\text{X})$ distributions observed in laser induced fluorescence. These researchers also suggest that some of the acrolein isomerizes to methylketene before dissociation.

Finally, a PTS study of H atom elimination from acrolein excited at 193 nm, using the high resolution Rydberg tagging method, was recently reported.³⁸ By comparison with methyl vinyl ketone, it was proven that it is the aldehydic H atom that is lost. Based upon H atom translational energy distributions which suggest a small barrier in the exit channel, these researchers proposed a dissociation mechanism which includes $T_1(\text{}^3n\pi^*)$ triplet state dissociation to form an excited state $\text{CH}_2\text{CHO}(\text{}^2\text{A}'')$ radical plus an H atom.

In the first part of this paper, we present a fs TRPES study of ultrafast non-adiabatic dynamics in the α,β -enones acrolein (propenal, AC), crotonaldehyde (γ -methyl propenal, CR), methyl vinyl

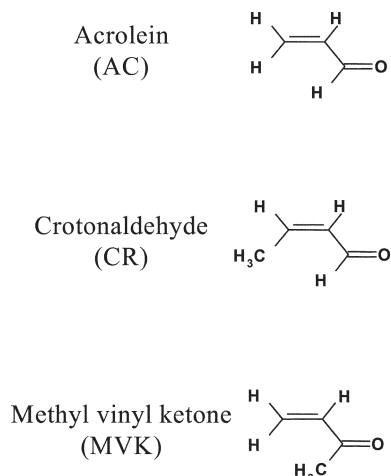


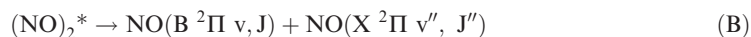
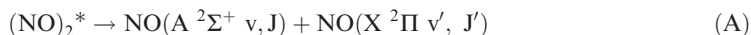
Fig. 2 Structures of the three α,β -enones used in these studies. The location of the methyl group has a dramatic effect on the relative non-adiabatic rates and product branching ratios.

ketone (α -methyl propenal, MVK), whose structures are shown in Fig. 2. By following the time evolution of the photoelectron spectra, we hope to discern the competing electronic relaxation processes in these molecules. We will show that the location of the methyl group has very dramatic effects on the relative rates of electronic processes. We corroborate these results with an absorption spectroscopy and laser induced fluorescence study of the relative HCO(X) yields from AC and CR, showing very dramatic changes in the HCO yield depending on the methyl location.

III. Ultrafast non-adiabatic photodissociation dynamics: The nitric oxide dimer

As an example of the use of TRPES in studying non-adiabatic photodissociation dynamics, we consider the case of the weakly bound *cis*-planar (C_{2v}) nitric oxide dimer. The weak ($D_0 = 710 \text{ cm}^{-1}$) 1A_1 ground state covalent bond is formed by the pairing of two singly occupied π^* orbitals, one from each NO($X^2\Pi$) monomer. The very intense UV absorption spectrum of the NO dimer is apparently broad and featureless^{40,41} and spans a 190–240 nm range, with a maximum at ~ 205 nm. This transition has been assigned as $^1B_2 \leftarrow ^1A_1$ and is of a parallel nature. *Ab initio* studies of the excited electronic states of the dimer revealed a very complex set of interactions which have yet to be fully untangled.^{42,43} The apparent lack of spectroscopic features was recently corroborated by a molecular beam resonance-enhanced multiphoton ionisation spectroscopic study of NO dimer photoabsorption in the 242–221 nm range.⁴⁴ These researchers also describe preliminary *ab initio* calculations (EOM-CCSD using the $6-311(2+,2+)G^{**}$ and $6-311(2+,2+)G(2df,2pd)$ basis sets) which identified two very strongly absorbing states (at 6.1 eV with $f \sim 0.45$ and 6.4 eV with $f \sim 0.2$, vertical excitation) of mixed valence/Rydberg character.⁴⁴ These ‘diabatic’ states are roughly comprised of a diffuse $3p_x$ Rydberg function (along the N–N bond) and a localized valence function. Most likely the valence function carries most of the oscillator strength in the Franck–Condon region, as the oscillator strengths are much too high for a pure Rydberg state. The lack of discernible vibrational structure in the absorption spectrum suggests that the electronic decoherence time of the initially prepared optically bright state is less than 50 fs.

Studies of the photodissociation dynamics at 193 nm revealed that two product channels are open:^{45,46}



The enthalpies of formation, relative to the ground state, for product channels (A) and (B) are 128.4 and 132.1 kcal mol⁻¹, respectively. The observed NO(A, B) product state distributions were

quite broad and appeared to be statistical. Subsequent studies on the alignment and vector correlations⁴⁷ of the excited state products showed only quite weak effects, supporting the notion of a statistical dissociation. The NO(A) + NO(X) product elimination channel, its scalar and vector properties and its evolution on the femtosecond time scale have been discussed in a number of recent publications.^{48–52}

A TRPES study of NO dimer photodissociation dynamics at 210 nm⁴⁸ excitation (287 nm probe) showed that the decaying (NO)₂⁺ parent ion signal disappeared more rapidly (fit to a single exponential decay of 0.3 ps) than the NO(A) state product appeared to rise (fit to a single exponential growth of 0.7 ps). The NO(A, v, J) products produced a single sharp peak in the photoelectron spectrum, due to the well known $\Delta v = 0$ NO(A ²Σ⁺, v) → NO⁺(X ¹Σ⁺, v) ionizing transition.⁵³ This result showed that the time dependence of the parent ion signal alone is misleading. [Neither the ground state NO(X ²Π) nor the excited state NO(B ²Π) product are ionized at 287 nm]. The results were interpreted in terms of a two-step non-adiabatic mechanism: the decay of the (NO)₂⁺ state on a time scale of 0.3 ps, is to another configuration which has relatively poor ionisation cross section for formation of ground state (NO)₂⁺ parent ion, perhaps due to an unfavourable electronic configuration and poor Franck–Condon factors. This suggested why the parent ion signal decayed in 0.3 ps even though the molecule had not dissociated. In this model, the second configuration decays to the products on a longer time scale, yielding an overall single exponential growth time of about 0.7 ps. We note, however, that large but *adiabatic* changes in the mixing of electronic configurations upon large amplitude nuclear motion can also lead to variations in both Koopmans' correlations and Franck–Condon overlaps. A classic example of large but adiabatic changes in a Born–Oppenheimer electronic wavefunction is seen in ion pair states of diatomic molecules. We note that the TRPES method cannot easily discern these processes from non-adiabatic changes in the total electronic wavefunction.

Recently, frequency resolved nanosecond lasers and a molecular beam photofragment ion imaging technique were used for detailed quantum state resolved product state studies of the NO dimer excitation region just above the threshold of channel (A) (*i.e.* $\lambda < 223$ nm).^{51,52} These researchers concluded that the dissociation dynamics were similar to that observed in other weakly bound species: they exhibited restricted intramolecular vibrational energy redistribution (non-statistical pair-correlated NO(A) and NO(X) distributions) in the excited state.

Recent fs time-resolved ion and photoelectron imaging studies shed new light on the dissociation dynamics of the NO dimer.^{49,50} Using 200.5 nm excitation and 250–350 nm probing, these researchers observed that both the decaying NO dimer cation signal and the rising NO(A) photoelectron signal could be fit using a single exponential function with a ~ 200 fs time constant. Furthermore, it was observed that the emerging NO(A) photoelectron peak appeared to change shape and shift in energy (by 15–20 meV) during the ~ 300 fs cross-correlation overlap time. This was interpreted as evidence for formation of a previously unknown NO dimer electronic state of Rydberg 3s character. This proposed state, formed by decay of the initial bright 'valence' state, was expected to correlate directly to NO(A) + NO(X) products. The authors argue that, should such a 3s Rydberg state be formed, its time evolution would be hard to discern from the growth of the NO(A) product because the shift in its photoelectron spectrum would become progressively smaller as the excited state dissociates. In this interpretation, the apparent ~ 0.7 ps risetime of the NO(A) state signal seen at 210 nm excitation⁴⁸ is primarily due to the formation of the NO dimer Rydberg 3s state (which smoothly evolves into the free NO(A) photoelectron peak) and therefore there is no contradiction between the decay of the excited parent molecule and the appearance of the products. This simple picture assumes, by analogy with a dissociating diatomic molecule,⁵⁴ that the dissociative NO dimer 3s Rydberg potential and the dissociative NO dimer cation potential to which it ionizes are *parallel*—or at least that their difference potential exhibits no maxima (thus allowing a simple one-to-one correspondence between transition energy and internuclear coordinate). Due to the complex nature of the excited state, it would be surprising if there were no maxima in the cation *vs.* neutral state difference potential, although the difference potential should become smooth at large interfragment separations. In a most recent study,⁵⁰ the excitation laser wavelength was varied from 200 to 235 nm and the time dependence of the (NO)₂⁺ signal was modeled with single exponential kinetics, including the expected non-resonant two-photon ionisation (cross-correlation) contribution plus an *ad hoc* step function used to help fit the data. The authors fit a single exponential growth curve to the appearance of the NO dimer 3s Rydberg state.

The extracted time constants seem to match quite well the decay time constants of the $(\text{NO})_2^+$ signal. However, we note that the *ad hoc* step function (which serves to fit the long lived tails of the data) had as much as 10% amplitude in the reported fits: the extracted decay time constants reported in this paper will be very sensitive to this contribution. In their analysis, the authors assumed that there was no change in the *shape* of the broad, apparently featureless NO dimer 'valence' photoelectron spectrum which underlies the emerging NO(A) state and 3s Rydberg state peak at early times. Based upon the observation that the extracted time constants varied smoothly with excitation energy and exhibited no abrupt changes at the energetic thresholds for dissociation into NO(B) + NO(X), at 215 nm, and NO(A) + NO(X), at 223 nm, these authors suggested that the NO(X) + NO(X) dissociation channel may be the major channel.

In the second part of this paper, we present a detailed fs TRPES study of the dissociation dynamics of the nitric oxide dimer at 200 nm excitation, paying particular attention to features which emerge during the laser cross-correlation time. We also present preliminary fs CIS studies of NO dimer photodissociation at 209 nm. We show how the various time-resolved scalar and vector coincidence maps facilitate separation of the dissociative ionisation from product state detection channels.

IV. Experimental

The femtosecond time-resolved magnetic bottle photoelectron spectroscopy experiment has been described in detail elsewhere.⁵⁵ Briefly, amplified independently tunable (200–300 nm) femtosecond pump and probe laser pulses (60–150 fs, 0.1–5 μJ) were brought collinearly and co-propagating into the interaction region of a molecular beam magnetic bottle photoelectron spectrometer. A doubly skimmed continuous molecular beam of the molecule of interest, seeded in Helium, was introduced to the interaction region of the spectrometer. The experiments consisted of recording photoelectron spectra at a series of time delays between the pump and probe laser pulses. All TRPES spectra presented here had photoelectron signals arising from either the pump or probe laser alone dynamically subtracted.

Acrolein (AC), crotonaldehyde (CR), methyl vinyl ketone (MVK) were purchased from Aldrich and used without further purification. These samples were loaded into a glass 'bubbler', cooled to -30°C , seeded in several hundred Torr of helium expanded through a 0.5 mm continuous molecular beam nozzle. The source of the photoelectron signals from each sample was verified by time-of-flight mass spectrometry. No clusters or signals from neutral fragments were observed. The absolute time zero and laser cross-correlation were determined using non-resonant two-photon ionisation of xenon and nitric oxide. The latter also provided a well known photoelectron spectrum to calibrate the energy scale of the photoelectron spectrometer.

For the absolute UV absorption and HCO laser induced fluorescence measurements, acrolein (Aldrich) was separated from water and stabilizer (hydroquinone) by vacuum distillation at -30°C , and then kept at -24°C (vapor pressure ≈ 25 torr) during experiments. Crotonaldehyde (Fluka) was kept at room temperature (vapor pressure 32.5 torr) during the experiments. In the HCO yield experiments, 1000 Torr helium was bubbled through the sample and expanded through a pulsed valve (General Valve, diameter 0.5 mm).

An ArF excimer photolysis laser with 3–4 mJ pulse⁻¹ (beam size, 5 mm diameter) intersected the molecular jet ~ 1.5 cm from the nozzle. The energy of the photolysis laser was kept low to be within the linear range for HCO production. A frequency-doubled, Nd:YAG-pumped dye laser generated tunable UV pulses of energy 1–1.5 mJ pulse⁻¹ with a linewidth of 0.25 cm⁻¹. This laser beam was used to excite HCO (X) to the $\tilde{\text{B}}^2\text{A}'$ state. The laser pulses were spatially overlapped in the interaction region and were temporally separated by 0.5–1 μs during the recording of the HCO laser-induced fluorescence spectra. A photomultiplier with bandpass filters was used to detect the emission.

The absolute absorption cross sections at 193 nm of both molecules were measured using synchrotron radiation from the HF-CGM beam line at SRRC, Hsinchu, Taiwan. This beam line is equipped with a cylindrical grating (600 g mm⁻¹, focal length 6 m and slit width 50 μm) to cover wavelength range 105–230 nm at 0.02 nm resolution. A LiF window eliminated short-wavelength, high order light diffracted from the grating. We used a double beam absorption cell of 8.9 cm

length and simultaneously recorded the incident and transmitted light intensities to obtain the absorbance. The samples were purified at least twice *via* vacuum sublimation prior to use. The absolute wavelength positions were calibrated with lines of CO, NO and O₂ in the same wavelength region.

For the nitric oxide dimer experiments, pure nitric oxide (Matheson) was premixed with helium in a 30% concentration and continuously expanded through a 0.1 mm nozzle with a few hundred torr stagnation pressure. Under these conditions, the dimer signal was very small (much smaller than the monomer). However, this situation guaranteed the absence of higher clusters in the experiment. [Detailed studies of the pressure dependence of the signals confirmed that no higher clusters were present]. The wavelengths of the pump and probe lasers were $\lambda_{\text{pump}} = 200$ nm (6.20 eV) and $\lambda_{\text{probe}} = 266.7$ nm (4.65 eV), respectively. Using CaF₂ Brewster angle prism compressors for each laser, the pump–probe cross correlation width (instrumental response function) was reduced to ~ 170 fs (FWHM).

The CIS apparatus, described in detail elsewhere,^{16,17} consists of a molecular beam source, a differential pumping chamber and an ultrahigh vacuum detection chamber containing the electron and ion optics and the particle detectors. The skimmed molecular beam source was doubly differentially pumped and tightly collimated to approximately 1 mm diameter. The molecular beam is crossed with a laser beam in the interaction region, located between two grids. The electrons are collected using a simple three-grid, space-focused assembly and accelerated towards the electron detector. A DC voltage from -5 to -50 V is applied to the grid above the interaction region to extract the electrons. After the electrons are detected, a floating pulse of up to -400 V was applied to the grid above the interaction region to increase the acceleration of the ions and optimize the space focusing conditions. The two detectors currently in use consist of a z -stack of three microchannel plates followed by a wedge-and-strip anode. This allows for time and (x,y) position measurements of a particle arrival, thus determining the lab frame 3D recoil momentum vector for that particle. Note that full 3D momentum vector measurement is not the same as the more common 2D projection measurements using CCD camera based ion and electron imaging. In the latter case, an inversion technique must be used to construct the 3D distribution. This non-linear process can be noisy and works only in the limiting case of cylindrically symmetric recoil distributions. The sequence of data collection begins with a laser pulse. Electrons are extracted and, after hitting the detector, their position is determined by digitizing the charges on the three anode electrodes. The electron arrival time is measured separately from a pulse off the back of the channel plate stack. A 14-bit time-to-digital converter measures the electron flight time with an overall resolution of ~ 200 – 300 ps. After the electrons have been detected, about 100 ns after the laser pulse, a voltage pulse is applied to extract the ions. The ions are further accelerated in a second field, and then drift approximately 25 cm to the detector. The ions are detected in a manner similar to the electrons, but a wide range time-to-digital converter is used so that multiple ion masses, spanning a wide mass range, can be detected without requiring any changes to the ion optics. Custom hardware is used to determine when valid coincident data is present on all the detector components. When a valid coincidence is detected the computer is interrupted to read in the data. The maximum data rate is determined by consideration of the probability of false coincidences.

V. Ultrafast non-adiabatic intramolecular dynamics in acrolein, crotonaldehyde and methyl vinyl ketone

In Fig. 3 we show a schematic energy level diagram and expected Koopmans' correlations for TRPES experiments on the α,β -enones AC, CR and MVK. The details of the Koopmans' ionisation correlation analysis for the α,β -enones will be presented in a future publication.⁵⁶ The optically prepared S₂ state ionises into the D₀ ionisation continuum *via* a single probe photon, producing the photoelectron band ϵ_2 . Upon ultrafast IC to S₁, the change in electronic structure alters the Koopmans' ionisation correlations such that ionisation into the D₀ continuum is no longer favoured. In this case, two probe photons are absorbed, allowing energetic access to the D₁ continuum and producing a broad band of energetic electrons, ϵ_1 . Exactly this type of behaviour, switching from one-photon to two-photon ionisation upon S₂ \rightarrow S₁ IC, has been previously

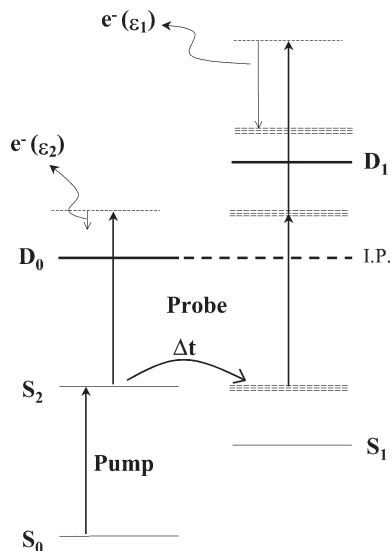


Fig. 3 A TRPES scheme for probing ultrafast non-adiabatic dynamics in the α,β -enones. A fs pump laser prepares the optically bright S_2 state which is expected to ionize into the D_0 ionization continuum, producing the photoelectron band ϵ_2 . Following ultrafast IC, the nascent, vibrationally excited S_1 state is expected to ionize *via* two-photon absorption into the D_1 ionization continuum, producing the photoelectron band ϵ_1 . By monitoring the photoelectron spectrum as a function of time delay between the fs pump and probe lasers, the excited state dynamics may be directly observed. For details, see the text.

observed and fully characterized in a detailed study of ultrafast IC in a linear polyene.^{15,57} Therefore, we expected that the optically prepared state produced, *via* single probe photon ionisation, a low energy photoelectron band ϵ_2 . Upon ultrafast IC, a higher energy photoelectron band ϵ_1 , due to two-photon probe ionisation, is expected to appear.

In Fig. 4, we present our experimental TRPES results for AC (top), CR (middle) and MVK (bottom), using 207.5 nm pump excitation and 280 nm probe ionisation. It can be seen that, in all three molecules, a low energy (< 1 eV) photoelectron band is produced at zero time delay. Based upon the known He photoelectron spectra^{29–31} and the pump and probe photon energies, this photoelectron band can, in all three cases, be assigned to the $S_2 \rightarrow D_0 + e^-$ ionisation transition, in agreement with the Koopmans' expectations. In each case, time-of-flight mass spectrometry was used to check that only the parent ion signal is observed, confirming the carrier of the spectrum. This S_2 photoelectron band decays very quickly, on a time scale close to the cross-correlation function response. The time evolution of the parent ion mass peak yielded time constants identical to those of the integrated S_2 photoelectron band, confirming the single probe photon ionisation picture shown in Fig. 3. By tuning just below the S_2 origin, a completely different photoelectron spectrum (very similar to the He photoelectron spectrum) was obtained. This demonstrates that the short-lived signal at low photoelectron energies is indeed due to resonant excitation of the S_2 state. As has been shown for numerous systems, energy integration across the photoelectron band yields the 'lifetime' of the zeroth order electronic state.⁵⁸ The ultrashort S_2 lifetimes extracted from a global fit to the time- and energy-resolved photoelectron spectra⁵⁶ were determined to be 30 ± 15 fs for AC, 20 ± 10 fs for CR and 35 ± 15 fs for MVK, as shown in Table 1. We attribute the ultrafast decay of the S_2 state to highly efficient IC to S_1 . This suggests the existence of an S_2 - S_1 CI near the S_2 minimum. In fact, at least one CI appears to exist in AC near the S_2 minimum which involves stretching and torsion of the ethylenic C=C bond.⁵⁹ Dynamical evolution (involving ethylenic torsion) through this CI should direct the system towards the bottom of the S_1 potential.

The broad high energy photoelectron bands seen in Fig. 4 are assigned to two-photon ionisation of the S_1 state formed by IC from S_2 . These spectra are complex and the full details of these assignments will be discussed elsewhere.⁵⁶ We note that in each case the width of the observed S_1 photoelectron spectrum corresponds to S_2 - S_1 vertical energy gap for that molecule. Furthermore,

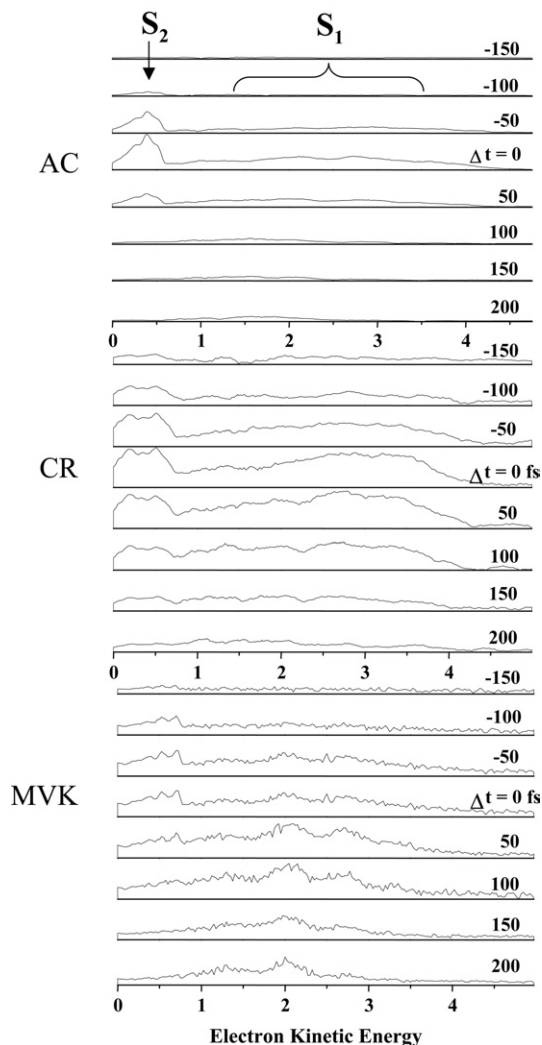


Fig. 4 Experimental TRPES results at $\lambda_{\text{pump}} = 207$ nm, $\lambda_{\text{probe}} = 280$ nm for acrolein (top), crotonaldehyde (middle) and methyl vinyl ketone (bottom). The low energy (< 1 eV) photoelectron bands correspond to ionization of S_2 . The time-delayed, very broad high energy photoelectron bands correspond to two-photon ionization of S_1 . Energy integration across each band yields the excited state lifetime for the state of concern. The results are presented in Table 1. For a discussion, see the text.

Table 1 Experimentally determined S_2 ($^1\pi\pi^*$) and S_1 ($^1n\pi^*$) lifetimes for acrolein (AC), crotonaldehyde (CR) and methyl vinyl ketone (MVK) using fs TRPES. The $S_2 \rightarrow S_1$ IC rates are sub-50 fs for all three molecules. The ISC rate for acrolein is from ref. 25. The estimated $S_1 \rightarrow S_0$ IC rates are given in the right hand column. Details are given in the text

	IC ($S_2 \rightarrow S_1$)	Experimental S_1 decay time	Estimated ISC ($S_1 \rightarrow T_2$)	Estimated IC ($S_1 \rightarrow S_0$)
AC	30 ± 15 fs	620 ± 60 fs	1.8 – 2.1 ps	650 ± 100 fs
CR	20 ± 10 fs	100 ± 20 fs	~ 2 ps	100 ± 20 fs
MVK	35 ± 15 fs	500 ± 60 fs	~ 2 ps	520 ± 100 fs

in all three cases there is a short (~ 30 fs) delay in the rise of the S_1 photoelectron band relative to the S_2 band, indicative of a sequential process. [We previously demonstrated reliable extraction of sub-50 fs excited state lifetimes from TRPES measurements⁵⁸]. Finally, the maximum observed photoelectron energy corresponds, in each case, to that expected from the known ionisation potential of the molecule and the absorption of one pump plus two probe photons. This demonstrates that no higher order processes are involved and supports the picture of two-probe photon detection of the S_1 state suggested by Fig. 3. These S_1 spectra also evolve very quickly, shifting towards lower electron kinetic energy at later times, indicative of large amplitude motion on the S_1 potential surface. The S_1 photoelectron spectra decay on a sub-ps time scale, presumably due to radiationless decay processes^{20,21} to the lower lying electronic state states T_2 , T_1 and S_0 . Energy integration across the broad S_1 photoelectron band and global analysis yields the zeroth order lifetime of the S_1 electronic state for each molecule.⁵⁶ The experimentally extracted S_1 time constants are 620 ± 60 fs for AC, 100 ± 20 fs for CR and 500 ± 60 fs for MVK, as shown in Table 1. Surprisingly, the experimental S_1 decay rate in CR is about *five times* faster than in either AC or CR.

We note that the S_1 - S_0 CI in AC lies about 30 kcal mol^{-1} below the S_2 - S_1 CI and is therefore fully accessible.⁵⁹ Furthermore, the S_1 - S_0 CI in AC lies about 15 kcal mol^{-1} above the S_1 minimum along an elongated and strongly twisted ethylenic C=C coordinate.²⁰ Therefore, we expect that the ethylenic C=C twisting (and extension) motions generated at the S_2 - S_1 CI will carry the system past the S_1 - S_0 CI point as it heads down towards the planar S_1 ($^1n\pi^*$) potential minimum. Near the S_1 potential minimum, an intersection with the T_2 ($^3\pi\pi^*$) state occurs and ultrafast ISC is expected.²⁰ Vibronic linewidth measurements suggested that the zeroth order lifetime at the S_1 state origin is ~ 2 ps.²⁵ Our TD/B3LYP/6-31G* calculations at the ground state geometry yield S_1 - T_2 energy gaps of 0.3 eV, 0.35 eV and 0.25 eV for AC, CR and MVK, respectively. (The spin-orbit coupling constant was likewise determined to be $\sim 67 \text{ cm}^{-1}$). Therefore, we do not expect large changes in the S_1 - T_2 ISC rates and assume that the rates in CR and MVK are comparable to those of AC. For the sake of further argument, we will set the ISC rates for all molecules to a limiting value of ~ 2 ps. If we assume that the experimentally observed sub-ps S_1 lifetimes are due to both S_1 - T_2 ISC and S_1 - S_0 IC processes, we can deconvolute the former from the latter to obtain estimated S_1 - S_0 IC rates for all three molecules. These are given in the last column of Table 1. It appears as if a specific methyl substitution on the ethylene end (*i.e.* CR) significantly increases the S_1 - S_0 IC rate relative to AC (no methyl) and MVK (methyl on the carbonyl end).

We note that at excitation energies corresponding to the S_2 state, the S_1 ($^1n\pi^*$) state can in principle dissociate *directly* to HCO plus vinyl radical products.²¹ In order to check this possibility, we looked for the appearance of any daughter fragments on the several ps time scale using time-resolved photoionisation mass spectrometry. None were observed, suggesting that there are no direct dissociation processes in these molecules on the ps time scale and therefore the experimentally observed S_1 decay rates reported in Table 1 likely indicate the dynamical processes assigned to them. Nevertheless, we would like to check using other, independent experiments that the S_1 - S_0 IC rate in CR is indeed much faster than in AC. This is described below.

In AC at both 300 nm and 193 nm excitation, significant HCO(X) plus vinyl radical photodissociation products were directly observed^{27,37} and were assumed to emanate from the triplet channels. The 193 nm photodissociation of MVK also produces vinyl radicals which (by analogy with AC) likely appear *via* triplet channels to produce vinyl plus CH_3CO , the latter dissociating to $\text{CH}_3 + \text{CO}$ —the final products observed in gas cell MVK photodissociation studies.⁶⁰ Assuming similar photochemistry for CR, one might also expect significant HCO elimination *via* triplet channels. However, the apparent five-fold increase in $S_1 \rightarrow S_0$ IC rate in CR (relative to AC) should compete very strongly with $S_1 \rightarrow T_2$ ISC. This leads to the prediction that the HCO yield from CR should be significantly less than that from AC. In order to test this, the relative HCO yields from 193 nm photodissociation of these two molecules were quantitatively determined, as described in the following.

The measured *absolute* UV absorption cross sections of AC and CR in the 120–220 nm wavelength range are shown in Fig. 5. The diffuse band lying at 180–220 nm is assigned to the S_2 - S_0 transition. The structure of this band indicates a short-lived excited state. At 193 nm the cross sections are measured to be 52.7 and 32.5 Mb for AC and CR, respectively. The laser-induced fluorescence spectra of HCO (X, v , J) photoproducts produced from 193 nm photolysis of AC

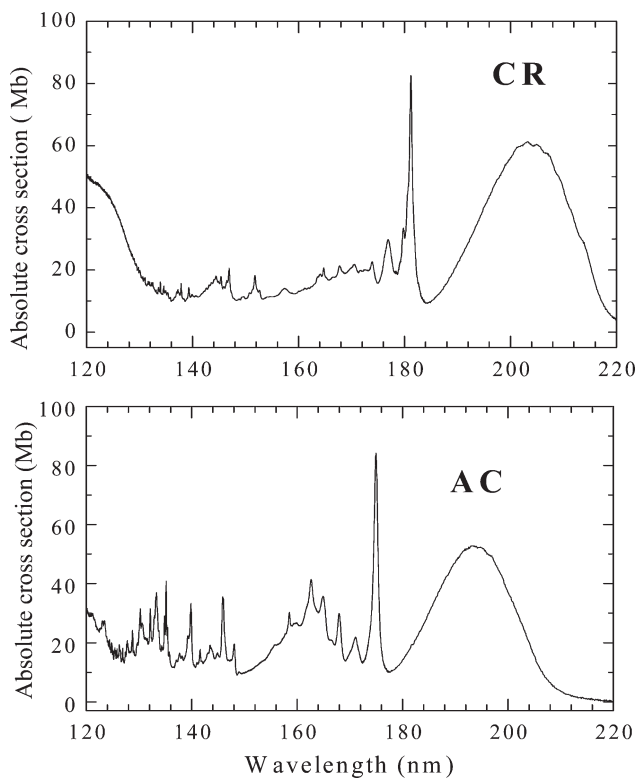


Fig. 5 Absolute UV absorption cross-section measurements for room temperature acrolein and crotonaldehyde. These are used to determine the relative absolute photochemical yields for the two molecules.

(bottom) and CR (top), shown near the bandhead region of the $\tilde{B}^2A' - \tilde{X}^2A'$ transition, are displayed in Fig. 6. The signal intensity of HCO from CR photodissociation is very small, close to the experimental noise limit. In order to obtain quantitatively the relative HCO(X) yields from AC and CR, we assumed that the internal state distributions of HCO products from each molecule are similar. By taking the ratio of the fluorescence intensity of the most intense HCO signal from AC photolysis to the average baseline observed in CR photolysis, the known relative number densities

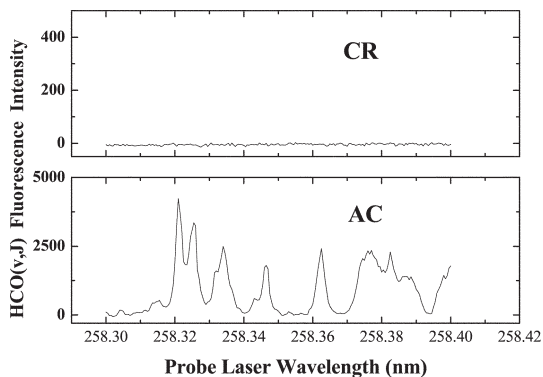


Fig. 6 Molecular beam laser-induced fluorescence determination of HCO(X, v, J) radical products from 193 nm photodissociation of acrolein (bottom) and crotonaldehyde (top). The absolute cross section for HCO(X) formation from CR is determined to be less than 0.35% of that from AC.

in the laser focus, the known absolute absorption cross-sections and laser powers, we have determined that the absolute cross-section for HCO formation from CR is less than 0.35% that of AC. This dramatically demonstrates that the location of the methyl group has a large effect on the relative rates of the non-adiabatic dissociation processes involved. It also supports the picture developed from the TRPES experiments described above that the competition between singlet and triplet channel electronic relaxation rates is significantly altered by the location of the methyl group.

In the absence of detailed *ab initio* molecular dynamics calculations, we are left but to speculate as to the origin of these dramatic effects. We do not believe that significant changes in the ISC rates can explain these results. Nor can simple density-of-states arguments explain these results because, at the internal energies of concern here (~ 6 eV), CR and MVK should have very similar vibrational state densities as they have an identical number of vibrational degrees of freedom. One possibility is that in AC there may be two kinds of CI close to the S_2 origin, one involving torsion about the ethylenic carbon and the other about the central carbon.⁵⁹ It is possible that these are favoured differently in CR, leading to a differing decay dynamics which perhaps avoids the triplet channels—however, this remains to be confirmed.

A very interesting speculation for the purposes of this Discussion is that the observed differences in singlet–triplet branching ratios are due to changes in diabatic *vs.* adiabatic branching dynamics at the S_1 – S_0 CI. By analogy with the one dimensional Landau–Zener problem, ‘the surface hopping’ probability (IC rate) is very sensitive to small changes in the relative ‘slopes’ of the ‘diabats’ (*i.e.* the shape of the CI) and the ‘velocity’ of the trajectory as it crosses the ‘gap’. Although there is no ‘gap’ in CIs, we still expect that the diabatic *vs.* adiabatic branching ratio will be sensitive to the ‘tilt’ of the CI cone axis relative to the trajectory velocity vector and to the magnitude of this ‘sub-space’ velocity as it traverses the CI region.

Within a simple biradicaloid picture,⁶¹ the shape of the $S_1 \rightarrow S_0$ CI depends on the electronegativity difference between the orbitals localized on either end of the molecule and their coupling. A methyl substituent is electron withdrawing and, therefore, the methylated end becomes more electronegative. This could affect the shape of the $S_1 \rightarrow S_0$ CI in CR *vs.* that in AC and MVK (these latter two having quite similar electronegativity differences but opposite in sign to that in CR). Another consideration is that the ‘velocity’ of the trajectory in the CI sub-space may be different in CR *vs.* AC. The $S_1 \rightarrow S_0$ CI involves the ethylenic torsion coordinate. This torsion is initiated at the $S_2 \rightarrow S_1$ CI and launches the trajectory down the S_1 potential surface where it passes, now with significant ‘torsional velocity’, through the S_1 – S_0 CI region. If this torsional velocity is high and the CI cone axis is tilted with respect to this vector, we might expect more adiabatic behaviour and the system prefers to remain on the S_1 surface. As the $S_1 \rightarrow T_2$ ISC rates are very high in these molecules, there are not many chances for re-crossing this CI before the system ends up in the triplet manifold. On the other hand, if the torsional velocity is lower, the behaviour may be more adiabatic and the crossing probability to S_0 is increased. In CR, the addition of a methyl group to the ethylenic end of the C=C bond very significantly changes the torsional frequency (‘velocity’). Based upon the change in the reduced mass of this coordinate, we expect a ~ 2 fold drop in this torsional frequency in CR relative to AC. If the simple Landau–Zener formula applied, this could result in an e^2 (~ 5) fold change in diabatic *vs.* adiabatic branching probabilities, consistent with our observations. In the above, we do not wish to imply that the dynamics are so simple. Rather, we wanted to use this over-simplified model to stimulate further discussion regarding the effects of vibrational dynamics on diabatic *vs.* adiabatic branching ratios at tilted CIs.

VI. Ultrafast non-adiabatic photodissociation dynamics of (NO)₂

In Fig. 7 we present a global overview of the TRPES results obtained for 200 nm photodissociation of the NO dimer. This 2D time- and energy-resolved surface plot displays the time dependent photoelectron spectra for pump–probe time delays ranging from -450 fs to $+2000$ fs, after subtraction of all single-laser signals as well as the non-resonant pump–probe contribution from NO monomers which always exist in the molecular beam. The spectral intensities are plotted as a function of the binding energy, derived by subtracting the electron kinetic energy from the sum of the pump and probe photon energies: $E_{\text{bin}} = 10.85 \text{ eV} - E_{\text{kin}}$. One can readily distinguish two

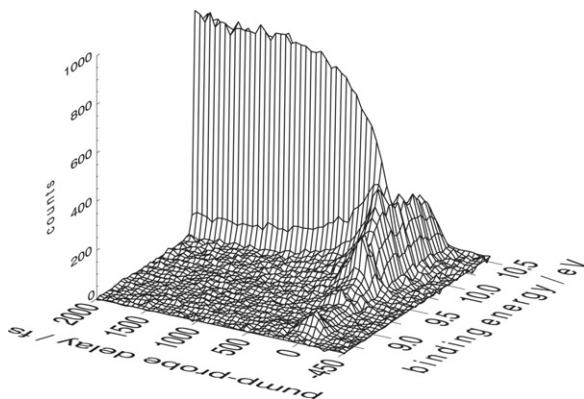


Fig. 7 A global 2D TRPES surface plot, showing photoelectron intensity as a function of binding energy and fs pump–probe time delay for $(\text{NO})_2$ excitation at $\lambda_{\text{pump}} = 200$ nm and ionization with $\lambda_{\text{probe}} = 266.7$ nm. The sharp ridge which grows at 10 eV binding energy is due to formation of the NO(A) photoproduct. The very broad, decaying photoelectron spectrum is due to photoionization of the $(\text{NO})_2$ excited state(s). For details, see the text.

major features: (1) A sharp peak at $E_{\text{bin}} \approx 10$ eV which grows with increasing pump–probe delay and reaches its asymptotic value by ~ 1 ps; (2) A broad spectrum ranging from $E_{\text{bin}} \approx 8.75$ eV up to the maximum binding energy which we were able to measure (≈ 10.5 eV). This broad photoelectron spectrum has its maximum intensity near zero pump–probe time delay and decreases with increasing time delay. [The observed maximum measured binding energy is not exactly equal to the sum of the pump and probe photon energies due to the transmission function of the magnetic bottle spectrometer which, at low energy, decreases with decreasing electron kinetic energy]. The sharp rising feature (1) is assigned to the photoelectron spectrum of the NO(A) photofragment which emerges after resonant excitation of the dimer. It is also important to note that, at these wavelengths, *very* little $(\text{NO})_2^+$ cation signal is observed (*via* mass spectrometry) relative to NO^+ , meaning that the strongly favoured ionisation transition is to a dissociative ionisation channel forming $\text{NO}^+ + \text{NO}(\text{X})$.

The broad spectrum (2) arises from the probe laser ionisation of excited dimer configurations which are either directly optically prepared, or which appear as an intermediate step between the initially excited dimer state and the emission of the final product states. As in all femtosecond pump–probe experiments, the broad spectrum can also, in principle, contain contributions from direct non-resonant two-photon ionisation of the dimer, as the Rabi rates in femtosecond laser experiments can be sufficiently high to generate non-resonant signals. In TRPES experiments, these non-resonant contributions are usually readily distinguished because they always follow the time-dependence of laser cross-correlation function and have the (time-independent) photoelectron spectrum of the neutral ground state.

In the following, we attempt to gain a deeper understanding of the dissociation process of the NO dimer upon resonant excitation at 200 nm and to develop a model consistent with all available experimental results. For any global analysis of the 2D data presented in Fig. 7, two basic questions must be addressed: (1) How many independent transients (with different time constants) need to be employed in order to model the dynamics in all spectral ranges? (2) How well do any extracted time constants for the decaying regions of the 2D spectrum correspond to the growth time constant of the rising NO(A) + NO(X) product channel signal? In order to address question (1), we deconvoluted the observed transients in different parts of the 2D spectrum through global non-linear least-square fits. Various 2D fits were performed using transient functions with differing numbers of independent components (of different time constants). We have determined that these data can be numerically modeled equally well (*i.e.* of comparable reduced χ^2) by two quite different physical models: a non-sequential ('parallel') model and a sequential model. In the parallel model (*i.e.* $[\text{Z}] \leftarrow [\text{X}^*] \rightarrow [\text{Y}]$), the data were fit to a sum of decaying and rising signals, all beginning at zero time delay, each described by a single exponential function. The physical meaning of the parallel

model is that two independent configurations are optically prepared *within* the ~ 120 fs pump laser pulse and that these channels evolve independently, one of them generating the observable NO(A) state products. This model does not preclude the possibility that the optically prepared bright state $[X^*]$ electronically dephases on a sub-50 fs time scale (as the absorption spectrum might suggest)—in this case, the independent evolution simply begins after this initial dephasing. In the sequential model (*i.e.* $[X^*] \rightarrow [Y] \rightarrow [Z]$), the data were fit to a sum of decaying and rising signals described by multiexponential functions with interdependent time constants. The physical meaning of the sequential model is that an initially prepared optically bright state decays to an intermediate state which subsequently decays to the observable NO(A) products. This model also does not preclude the possibility that the optically prepared bright state $[X^*]$ electronically dephases on a sub-50 fs time scale. All transient functions were convoluted with the measured Gaussian cross-correlation function (170 fs FWHM).

Two numerical fitting procedures, global fitting and singular value decomposition, are commonly used to fit 2D data of the sort discussed here but do not always lead to the unambiguous interpretation of real experimental data. Real data contain noise and, especially if there are components with comparable time constants but greatly different amplitudes, the results of the fitting procedure may be quite sensitive to the initial input values used. As the convolution of several exponential functions is very sensitive to slight variations in the data, it is recommended that the fitting procedure be performed in two steps.⁶² In the first step, all amplitudes and time constants of all transient components were free parameters. In the second step, the time constants were fixed to a few average values derived in the first step and only the amplitudes of the different components were allowed to vary.

In Fig. 8 we illustrate the deconvolution of transients in two different spectral regions through a global fit using the sequential model. Three components were used for the global fits: a single exponential decay with a time constant of $\tau_1 = 110$ fs, an intermediate component which is populated by this single exponential decay but itself decays with a $\tau_2 = 380$ fs time constant, and, finally, a third (rising) component for the emergence of the final product state. The dashed lines show the individual components whereas the solid lines show their sums. The inserts in the plots are contour maps of the 2D data shown in Fig. 7. The vertical dashed lines on each contour map mark the ranges over which the data were integrated in order to derive the transients shown in Fig. 8. It is important to note that the plots shown in Fig. 8 are only two illustrative examples from a whole series of fits using different models, applied to all regions of the photoelectron spectrum, as discussed above. A detailed description of the results for different fit procedures and different photoelectron spectrum integration ranges used to generate the transients will be given elsewhere.⁶³

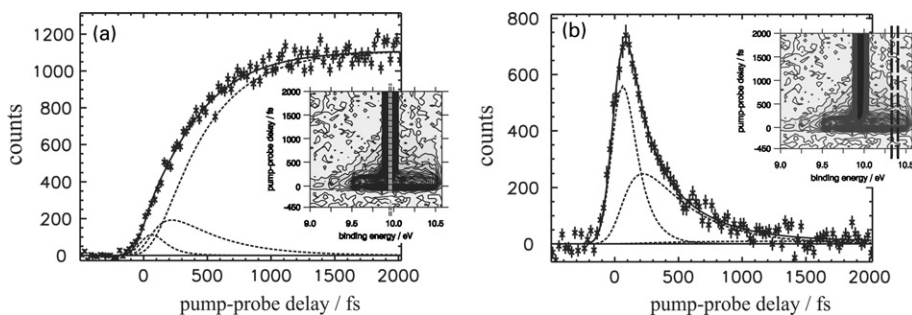


Fig. 8 Non-linear least squares 2D global fits to the transients as a function of time delay and photoelectron binding energy, presented here for a sequential dynamics model. We show two 1D slices of these fits for two different energy regions of the photoelectron spectra: (a) at $E_{\text{bind}} \sim 10$ eV where the formation of the NO(A) product is observed; and (b) at $E_{\text{bind}} \sim 10.3$ eV where aspects of the $(\text{NO})_2^*$ decay dynamics are observed. [The inserts are contour map versions of the 2D data shown in Fig. 7. The energy integration ranges used to generate these 1D plots are shown as vertical lines, in each case]. The dashed lines in the fits are the different time dependent transient functions used in the sequential model, the solid lines are the sums of the dashed lines and fit the experimental data well (at all times and photoelectron energies). All transient functions were convoluted with the laser cross correlation function. See the text for details.

We present two important conclusions, nicely foreshadowed in Fig. 8, which emerge from *all* the different fitting procedures we employed. (1) It is *not* possible to give a satisfactory description of the decaying portion of the photoelectron spectrum using only one single component with one single decay time constant. At least two components with significantly different time constants ($\tau_1 \approx 100$ fs, $\tau_2 \approx 400$ fs) must be used in order to achieve good global agreement between the fit and the measured transients. This is in disagreement with previous studies that used only single exponential fits.^{48–50} (2) The rise time of the NO(A) channel signal agrees well with the decay time τ_2 of the slowly decaying component of the broad spectrum but is significantly different from the decay time of the photoelectron peaks associated with the bound dimer cation (which can be almost entirely described by the short decay time τ_1). This confirms the earlier TRPES experimental observations at 210 nm on this system.⁴⁸ In the analysis it is important to take into account that the signal within the spectral range of the NO(A) channel peak is the sum of the rising NO(A) channel signal and the decaying signals from all other excited state NO dimer channels. In other words, the decaying channels present a time varying ‘background’ lying underneath the growing NO(A) channel signal. This complicates the interpretation of the observed peak shift as simply a change in the NO(A) channel peak shape at early times.^{49,50} Again we emphasize that the dominant contribution to the broad photoelectron spectrum is the dissociative ionization channel. In a future publication we will describe the details of this analysis.⁶³

The two conclusions above hold true independent of whether the applied model is for a parallel or a sequential decay mechanism. This means that, on a purely numerical basis, we *cannot* decide from our data alone whether the excited dimer state decays directly into the NO(A) + NO(X) channel or if this final state achieves *via* an intermediate configuration. The two kinetic models, parallel and sequential, for the conceivable reaction pathways are shown in Fig. 9. In either model, it is seems likely that the slowly decaying component of the NO dimer photoelectron spectrum is the channel which populates the final NO(A) + NO(X) product channel.

In the case of the parallel model, two excited dimer states are prepared within the ~ 120 fs pump pulse duration. One state $(\text{NO})_2^{*1}$, decays with a time constant of $\tau_1 \approx 100$ fs towards a channel which we cannot detect in our measurements (conceivably the NO(B) + NO(X) channel). The other state $(\text{NO})_2^{*2}$ decays into the NO(A) + NO(X) product channel with a $\tau_2 \approx 400$ fs time constant. In the case of the sequential model, an initially prepared state $(\text{NO})_2^{*1}$ decays within $\tau_1 \approx 100$ fs into an intermediate state $(\text{NO})_2^{*2}$ which subsequently decays into the NO(A) + NO(X) product channel with a time constant of $\tau_2 \approx 400$ fs. Since we cannot decide by the quality of the fits alone which model is closer to reality, we must find other arguments either for or against the models and/or perform experiments which provide additional information complementary to our TRPES measurements.

A conceptual drawback of the parallel model is that it predicts two excited dimer states which are close enough in energy to be excited by the same laser pulse, yet have two quite different decay time constants. One might expect that states of the same symmetry lying so close in energy might be strongly vibronically coupled, leading to comparable decay times. This conceptual problem is somewhat diminished if there is an initial optically bright dimer excited state which electronically dephases into the two different parallel model excited states within a timescale which is small (< 50 fs) compared to our 170 fs cross-correlation time. Nevertheless, the need for spectroscopically dark

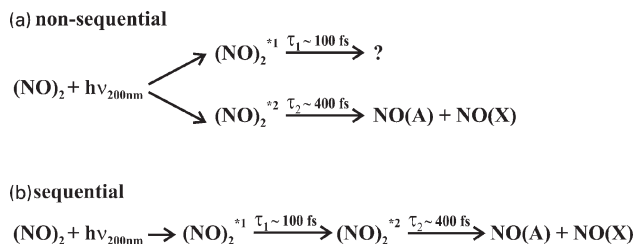


Fig. 9 Two different reaction kinetics mechanisms, a parallel model and a sequential model, present two different ways to fit the experimental data. Both models can fit the 2D data with equal reduced χ^2 . Their physical interpretation, however, is quite different. For details, see the text.

states and the difference in the two observed decay time scales make the parallel model seem *chemically* less appealing than the sequential model. The latter does not require any optically dark states. A problem for the sequential model, however, is the relatively long lifetime of the initially excited dimer state, about 100 fs, which is not in agreement with some previous estimates. From the absence of vibrational progressions in the absorption spectrum, it was argued that the excited dimer state is repulsive and rapidly decays into the final product states.^{40,41,45,46} Recent unpublished measurements using synchrotron radiation, however, did reveal vibrational structure in the photofragment fluorescence yield action spectrum.⁶⁴ This vibrational structure is quite different from that of the cation ground state, suggesting that the excited state is predominantly of valence rather than Rydberg character. Nevertheless, the action spectrum does *not* provide direct information about the absorption spectrum and there remains a need for a high quality molecular beam direct UV absorption measurement.

In addition to the TRPES experiments, we performed a coincident imaging spectroscopy (CIS) experiment using pump- and probe-pulse wavelengths (photon energies) of $\lambda_{\text{pump}} = 209$ nm (5.93 eV) and $\lambda_{\text{probe}} = 278$ nm (4.46 eV), respectively. The coincident detection of photoelectrons and photoions in the CIS experiment enables us to gain information inaccessible *via* photoelectron or ion spectroscopy alone. In Fig. 10, we show two scalar coincidence correlation maps (photoelectron *vs.* photoion kinetic energy) measured at pump–probe delays of 200 fs, Fig. 10(a), and 1000 fs, Fig. 10(b). The contour maps show the coincidence intensity between photoelectrons and photofragment NO^+ ions, as a function of the total kinetic energy release (KER) of both monomer fragments (horizontal axis) and the kinetic energy of the photoelectrons (vertical axis). We emphasize again that by far the most dominant NO dimer channel observed is the dissociative ionization process producing $\text{NO}^+ + \text{NO}(\text{X})$. Integrating the contour maps along the two different axes leads to the total electron- and ion-kinetic-energy spectra, shown to the left and below each contour map. These are the spectra that would normally be seen in non-coincident photoelectron and/or photoion spectroscopy experiments. Their overall shapes can be compared with the results of other groups using non-coincident imaging techniques to measure the kinetic energy distributions. To the best of our knowledge there are no comparable spectra published for a pump

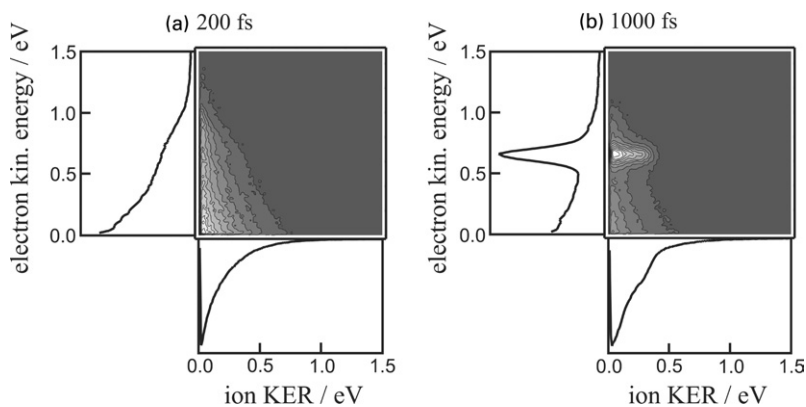


Fig. 10 Coincidence imaging spectroscopy study of $(\text{NO})_2$ photodissociation dynamics using $\lambda_{\text{pump}} = 209$ nm and $\lambda_{\text{probe}} = 278$ nm. Full 3D lab frame momentum vectors of photoelectrons and photofragments are detected in coincidence, allowing for both scalar and vector correlations to be measured as a function of time. Here we show photoelectron energy–photofragment kinetic energy (scalar) correlation maps at two different pump–probe time delays: 200 fs (left), and 1000 fs (right). The maps show the coincidence intensity of photoelectrons and fragment NO^+ ions as a function of (horizontal axis) the total kinetic energy release (KER) of both monomer fragments and (vertical axis) the kinetic energy of the photoelectrons. The plots on the sides of each contour map show the total intensities of photoelectrons (left) and photofragment ions (bottom) obtained by integration over the complementary coordinate. These would be the results obtainable *via* non-coincident ion or electron measurements. At 200 fs delay, the dissociative ionization channel of the NO dimer excited state is dominant. At 1000 fs delay, the $\text{NO}(\text{A})$ photofragment is seen to appear and has a different KER spectrum than that of the dissociative ionization channel. For details, see the text.

wavelength of 209 nm. However, the results at 200.5 nm⁴⁹ and at 228 nm⁴⁴ excitation generally agree with the integrated spectra shown in Fig. 10.

One interesting characteristic of the energy correlation map shown in Fig. 10 (a) is, that, even in coincidence, the electron and ion kinetic energies peak near zero energy. In other words, the slower the emitted photoelectron, the slower the emitted photofragment ion. From the coincident data shown in Fig. 10(a), it seems that the main portion of the energy difference between the dimer ionic state and the final dissociated state is deposited into the internal degrees of freedom of the NO monomer fragments, in agreement with previous observations.^{44,49,51,52}

The map shown in Fig. 10(b) is dominated by a correlation peak at a photoelectron kinetic energy of 0.66 eV. From the discussion of the TRPES experiment above, it is clear that this peak is due to NO dimer photodissociation followed by the ionisation of the NO(A) photofragment. Although the smooth background from the dimer dissociative ionisation still has to be subtracted, Fig. 10(b) already shows that the kinetic energy distribution of the NO(A) photofragments is significantly different from the NO⁺(X) fragments produced in the dissociative ionisation process. Furthermore, we note that the raw data recorded by the CIS method are fully three dimensional. In other words, for each data point on the correlation map shown in Fig. 10, there is also *coincident* information (not shown here) about the lab frame recoil angles of both the photoelectron and the photoion. In the next step of analysis, we will derive the photoelectron and ion emission angular distributions associated with different regions of the correlation maps. This additional angular information may help discern the different channels of NO dimer photodissociation. In addition, this approach could provide a view of the photofragment angular momentum polarization and v - J correlations as a function of time during unimolecular decay. In the energy domain, atomic angular momentum polarization measurements have shown sensitivity to details of the photodissociation dynamics.⁶⁵ Time domain measurements could give a new perspective on non-adiabatic unimolecular decay dynamics. This highly differential time-resolved information will hopefully enable us to reveal further details about the dynamics of the reaction and the symmetries of the states involved in the different reaction pathways.

VII. Conclusions

We have attempted to demonstrate that TRPES (time-resolved photoelectron spectroscopy) and CIS (coincidence imaging spectroscopy) experiments can provide new insights into the complex non-adiabatic intramolecular and photodissociation dynamics of photoexcited polyatomic molecules. Using the α,β -enones as an example of intramolecular dynamics, we measured S_2 and S_1 lifetimes and observed dramatic effects due to the location of a methyl substituent. The $S_1 \rightarrow S_0$ IC rate in CR was five times faster than that in either AC or CR. This led to the prediction that little HCO product would be observed from CR photolysis as compared with AC. This was confirmed by absolute HCO yield measurements. We speculated on the interesting possibility that these results may be related to diabatic *vs.* adiabatic branching at tilted conical intersections due to vibrational dynamics effects.

We studied the non-adiabatic UV photodissociation dynamics of the NO dimer using both TRPES and CIS methods. For the 200 nm photodissociation of (NO)₂, we clearly identified two different timescales, showing that the results could not be fit with a single exponential function. We could globally fit the observations with either a parallel or a sequential model scheme. CIS gives access to highly differential time-resolved information on the energetics, symmetries and vector properties of the product states. As such, we expect that it holds much promise for the study of complex reaction mechanisms.

We believe that we are at the dawn of a renaissance in experimental and theoretical studies of non-adiabatic molecular dynamics. However, there is still a great need for *ab initio* molecular dynamics calculations on ultrafast non-adiabatic processes such as the ones described here. In order to properly model the results of fs TRPES and CIS experiments, one will eventually need potentials, their non-adiabatic couplings and multi-mode dynamical propagation schemes as well as cation potentials and Koopmans'-type ionisation correlations. We hope that this Discussion will help stimulate more interest in these joint experimental-theoretical problems. The simple rules have yet to be worked out.

Acknowledgements

The authors thank Dr Y. Naitoh for providing his unpublished NO dimer action spectrum and for helpful discussions. We thank Prof. Massimo Olivucci for useful discussions on acrolein photo-physics and for sharing his preliminary *ab initio* results on this system. We thank Prof. Hanna Reisler for providing preprints of her work and for discussions on NO dimer photodissociation dynamics. A. S. thanks Prof. W. Domcke and Prof. T. J. Martinez for helpful discussions on non-adiabatic dynamics in polyatomic molecules.

References

- 1 J. Michl and V. Bonacic-Koutecky, *Electronic Aspects of Organic Photochemistry*, Wiley, New York, 1990.
- 2 For example J. Kommandeur, W. A. Majewski, W. L. Meerts and D. W. Pratt, *Ann. Rev. Phys. Chem.*, 1987, **38**, 433.
- 3 For example G. Orlandi, F. Zerbetto and M. Z. Zgierski, *Chem. Rev.*, 1991, **91**, 867.
- 4 For example G. Stock and W. Domcke, *Adv. Chem. Phys.*, 1997, **100**, 1.
- 5 For example M. Garavelli, F. Bernardi, M. Olivucci, T. Vreven, S. Klein, P. Celani and M. A. Robb, *Faraday Discuss.*, 1998, **110**, 51.
- 6 For example M. Ben-Nun and T. J. Martínez, *Adv. Chem. Phys.*, 2002, **121**, 439.
- 7 R. Schinke, *Photodissociation Dynamics*, Cambridge University Press, 1993.
- 8 L. J. Butler, *Ann. Rev. Phys. Chem.*, 1998, **49**, 125.
- 9 A. Stolow, *Ann. Rev. Phys. Chem.*, 2003, **54**, 89.
- 10 A. Stolow, *Int. Rev. Phys. Chem.*, 2003, **22**, 377.
- 11 A. Stolow, A. E. Bragg and D. M. Neumark, *Chem. Rev.*, 2004, in press.
- 12 C. C. Hayden and A. Stolow, in *Advanced Physical Chemistry*, ed. C.-Y. Ng, World Scientific., Singapore, 2000, vol. 10.
- 13 V. Blanchet, S. Lochbrunner, M. Schmitt, J. P. Shaffer, J. J. Larsen, M. Z. Zgierski, T. Seideman and A. Stolow, *Faraday Discuss.*, 2000, **115**, 33.
- 14 M. Seel and W. Domcke, *J. Chem. Phys.*, 1991, **95**, 7806.
- 15 V. Blanchet, M. Z. Zgierski, T. Seideman and A. Stolow, *Nature*, 1999, **401**, 52.
- 16 J. A. Davies, J. E. LeClair, R. E. Continetti and C. C. Hayden, *J. Chem. Phys.*, 1999, **111**, 1.
- 17 J. A. Davies, R. E. Continetti, D. W. Chandler and C. C. Hayden, *Phys. Rev. Lett.*, 2000, **84**, 5983.
- 18 A. D. Walsh, *Trans. Faraday Soc.*, 1946, **42**, 66.
- 19 S. Nagakura, *Mol. Phys.*, 1960, **3**, 105.
- 20 M. Reguero, M. Olivucci, F. Bernardi and M. A. Robb, *J. Am. Chem. Soc.*, 1994, **116**, 2103.
- 21 W.-H. Fang, *J. Am. Chem. Soc.*, 1999, **121**, 8376.
- 22 F. Aquilante, V. Barone and B. O. Roos, *J. Chem. Phys.*, 2003, **119**, 12 323.
- 23 M. F. Arendt, P. W. Browning and L. J. Butler, *J. Chem. Phys.*, 1995, **103**, 5877.
- 24 R. S. Becker, K. Inuzuka and J. King, *J. Chem. Phys.*, 1970, **52**, 5164.
- 25 K. S. Paulisse, T. O. Friday, M. L. Graske and W. F. Polik, *J. Chem. Phys.*, 2000, **113**, 184.
- 26 J. D. C. Brand and D. G. Williamson, *Trans. Faraday Soc.*, 1963, **35**, 184.
- 27 Y. T. Kao, W. C. Chen, C. H. Yu and I. C. Chen, *J. Chem. Phys.*, 2001, **114**, 8964.
- 28 H. van Dam and A. Oskam, *J. Electron Spectrosc. Relat. Phenom.*, 1978, **13**, 273.
- 29 P. Masclat and G. Mouvier, *J. Electron Spectrosc. Relat. Phenom.*, 1978, **14**, 77.
- 30 H. Bock, T. Hirabayashi and A. Semkow, *Chem. Ber.*, 1981, **114**, 2595.
- 31 H. Bock, S. Mohmand, T. Hirabayashi and A. Semkow, *Chem. Ber.*, 1982, **115**, 1339.
- 32 J. W. Coomber and J. N. Pitts, *J. Am. Chem. Soc.*, 1969, **91**, 547.
- 33 M. E. Umstead, R. G. Shortridge and M. C. Lin, *J. Phys. Chem.*, 1978, **82**, 1455.
- 34 H. Shinohara and N. Nishi, *J. Chem. Phys.*, 1982, **77**, 234.
- 35 G. T. Fujimoto, M. E. Umstead and M. C. Lin, *J. Chem. Phys.*, 1985, **82**, 3042.
- 36 B. M. Haas, T. K. Minton, P. Felder and J. R. Huber, *J. Phys. Chem.*, 1991, **95**, 5149.
- 37 S. H. Jen and I. C. Chen, *J. Chem. Phys.*, 1999, **111**, 8448.
- 38 B. F. Parsons, D. E. Szpumar and L. J. Butler, *J. Chem. Phys.*, 2002, **117**, 7889.
- 39 P. M. Regan, F. Qi, A. G. Suits, J. K. C. Lau and W. K. Li, unpublished.
- 40 J. Billingsley and A. B. Callear, *Trans. Faraday Soc.*, 1971, **67**, 589.
- 41 E. Forte and H. van den Berg, *Chem. Phys.*, 1978, **30**, 325.
- 42 A. L. L. East, *J. Chem. Phys.*, 1998, **109**, 2185.
- 43 R. Sayos, R. Valero, J. M. Anglada and M. Gonzalez, *J. Chem. Phys.*, 2000, **112**, 6608.
- 44 V. Dribinski, A. B. Potter, I. Federov and H. Reisler, *Chem. Phys. Lett.*, 2004, **385**, 233.
- 45 O. Kajimoto, K. Honma and T. Kobayashi, *J. Chem. Phys.*, 1985, **89**, 2725.
- 46 Y. Naitoh, Y. Fujimura, K. Honma and O. Kajimoto, *Chem. Phys. Lett.*, 1993, **205**, 423.
- 47 Y. Naitoh, Y. Fujimura, K. Honma and O. Kajimoto, *J. Chem. Phys.*, 1995, **99**, 13 652.
- 48 V. Blanchet and A. Stolow, *J. Chem. Phys.*, 1998, **108**, 4371.

- 49 M. Tsubouchi, C. A. de Lange and T. Suzuki, *J. Chem. Phys.*, 2003, **119**, 11 728.
50 M. Tsubouchi and T. Suzuki, *Chem. Phys. Lett.*, 2003, **382**, 418.
51 A. B. Potter, V. Dribinski, A. V. Demyanenko and H. Reisler, *J. Chem. Phys.*, 2003, **119**, 7197.
52 A. V. Demyanenko, A. B. Potter, V. Dribinski and H. Reisler, *J. Chem. Phys.*, 2003, **117**, 2568.
53 J. C. Miller and R. N. Compton, *J. Chem. Phys.*, 1981, **75**, 22.
54 M. T. Zanni, V. S. Batista, B. J. Greenblatt, W. H. Miller and D. M. Neumark, *J. Chem. Phys.*, 1999, **110**, 3748.
55 S. Lochbrunner *et al.*, *J. Electron Spectrosc. Relat. Phenom.*, 2000, **112**, 183.
56 J. P. Shafer *et al.*, in preparation.
57 V. Blanchet, M. Z. Zgierski and A. Stolow, *J. Chem. Phys.*, 2001, **114**, 1194.
58 S.-H. Lee, K.-C. Tang, I.-C. Chen, M. Schmitt and J.P. Shafer *et al.*, *J. Phys. Chem. A*, 2002, **106**, 8979.
59 M. Olivucci, personal communication.
60 A. Fahr, W. Braun and A. H. Laufer, *J. Phys. Chem.*, 1993, **97**, 1502.
61 V. Bonacic-Koutecky, J. Koutecky and J. Michl, *Angew. Chem. Int. Ed. Engl.*, 1987, **26**, 170.
62 H. Satzger and W. Zinth, *Chem. Phys.*, 2003, **295**, 287.
63 O. Geßner *et al.*, to be submitted.
64 Y. Naitoh, T. Ibuki and O. Kajimoto, personal communication.
65 For example Z. H. Kim, A. J. Alexander and R. N. Zare, *J. Phys. Chem. A*, 1999, **103**, 10 144.